A Hybrid Framework for Accurate Infant Brain Extraction from MRI

Amir Alansary, *Member, IEEE*, Ahmed Soliman, *Member, IEEE*, Fahmi Khalifa, *Member, IEEE*, Matthew Nitzken, *Member, IEEE*, Ahmed Elnakib, *Member, IEEE*, Manuel F. Casanova, and Ayman El-Baz*, *Member, IEEE*

Abstract—In this paper, we propose a novel framework for the automated extraction of the brain from T1-weighted MR images. The proposed approach is primarily based on the integration of a stochastic model (a two-level Markov-Gibbs random field (MGRF)) that serves to learn the visual appearance of the brain texture, and a geometric model (the brain iso-surfaces) that preserves the brain geometry during the extraction process. The proposed framework consists of four main steps: (*i*) Following brain intensity normalization, a new 3D MGRF having a 26-pairwise interaction model is applied to enhance the homogeneity of MR images and preserve the 3D edges between different brain tissues; (*ii*) The non-brain tissue found in the MR images is removed using the brain extraction tool (BET); (*iii*) The brain is then parceled to nested iso-surfaces using a fast marching level set method; (*iv*) Finally, a classification step is applied in order to accurately remove the remaining parts of the skull without distorting the brain geometry. The classification of each voxel found on the iso-surfaces is made based on the first- and second-order visual appearance features. The first-order visual appearance is estimated using a linear combination of discrete Gaussians (LCDG) to model the intensity distribution of the brain signals. The second-order visual appearance is constructed by using a MGRF model with analytically estimated parameters. The fusion of the LCDG and MGRF, along with their analytical estimation, allows the approach to be fast and accurate for use in clinical applications. The proposed approach was tested on *in-vivo* data using 300 infant 3D MR brain scans and validated using 9 data sets based on three metrics: the Dice coefficient, the 95-percentile modified Hausdorff distance, and absolute brain volume difference. We found that our approach is capable of outperforming four widely used brain extraction tools: BET, BET2, brain surface extractor (BSE), and infant brain extraction and analysis toolbox (iBEAT).

Index Terms—Infant Brain, Skull Stripping, MRI, MGRF, BET, Iso-surfaces.

I. INTRODUCTION

BRAIN extraction is the process of removing all the outer tissues (e.g. eyes, dura, scalp, and skull) around the brain, which consists of the gray matter (GM) and white matter (WM), while the inclusion of cerebrospinal fluid (CSF) in the brain depends on the application. Brain extraction is a primary step in neuroimaging analysis as well as a pre-processing step for many brain analysis algorithms like intensity normalization, registration, classification, and segmentation. Accordingly, accurate brain extraction is crucial for these algorithms to work properly. For instance, in cortical thickness estimation, inaccurate skull stripping (e.g. failing to remove the dura or missing brain parts) can result in an overestimation or underestimation of the cortical thickness [1].

Many brain extraction approaches have been developed to extract the brain from T1-weighted MR brain images. These methods use different techniques, such as, deformable models, atlas-based and label fusion, and hybrid algorithms. Smith [2] developed an automated deformable model-based method, which is widely known as the brain extraction tool (BET). In their approach, the deformable contour is guided by a set of locally adaptive forces, which include morphological and image-based terms in addition to a surface smoothness constraint. Liu et al. [3] presented another deformable model-based brain extraction method using a set of Wendland's radial basis functions [4]. Their deformable model is directed by an internal force to consider the smoothness constraint and an external force to impose the intensity contrast across the boundaries. Finally, they integrate the brain contours calculated separately on 2D coronal and sagittal slices to obtain a complete 3D brain volume. Also, Zhuang et al. [5] used a level set-based deformable model that combines two forces: the mean curvature of the curve and the intensity characteristics of the cortex in MR images. Baillard et al. [6] developed a deformable model-based approach to find the brain surface. As an alternative solution for initializing the first contour manually, an atlas-based technique is used to make the brain extraction process entirely automatic. After atlas registration and initial segmentation, the brain is finally segmented based on level sets that use adaptive parameters depending on the input data. Suresh et al. [7] presented a skull stripping approach using graph cuts, which consists of two steps. An initial brain mask is generated using intensity thresholding as a first step. Then, a graph theoretic image segmentation technique is applied to position cuts that isolate and remove narrow connections. Zhaung et al. [8] developed a simple method for brain extraction by estimating image intensity parameters to construct a binary image of the head. Then, an initial contour is estimated. The final brain is extracted using an improved geometric active contour model which extends the solution of the boundary leakage problem to be less sensitive to intensity inhomogeneity. Somasundaram et al. [9] developed a two-stage brain extraction method. First, they locate a region of interest using feature extraction to produce a

Amir Alansary, Ahmed Soliman, Matthew Nitzken, Fahmi Khalifa, and Ahmed Elnakib are with the BioImaging laboratory, Bioengineering Department, University of Louisville, Louisville, KY 40292, USA.

Manuel F. Casanova is with the Department of of Psychiatry and Behavioral Science, University of Louisville, Louisville, KY, USA.

*Ayman El-Baz is with the BioImaging laboratory, Bioengineering Department, University of Louisville, Louisville, KY 40292, USA (Corresponding author, e-mail: aselba01@exchange.louisville.edu).

rough brain segmentation. Then, the final brain segmentation is obtained using morphological operations in three steps: i) erosion, ii) brain area selection, and iii) dilation to generate the final brain mask. Leung et al. [10] presented a brain extraction technique using a template library. Multiple best-matched atlases are selected from comparing the target image to all the atlases in the template library. To segment the target image optimally after image registration and label propagation, label fusion techniques are used to combine the labels from different atlases. Iglesias et al. [11] developed a learning-based brain extraction system which combines two models: a discriminative model based on a random forest classifier trained to detect the brain boundary, and a generative model based on finding the contour with highest likelihood according to the discriminative model, which is refined later using graph cuts. Segonne et al. [12] presented a hybrid approach that combines watershed algorithms and deformable surface models. The watershed, with a preflooding height, construct an initial estimate of the brain volume using a single white matter voxel as a global minimum. Then, a surface deformation process is used to correct the initial segmentation inaccuracies. A statistical atlas is used finally to potentially correct the segmentation. Rex et al. [13] developed a meta-algorithm that uses four freely available brain extraction algorithms: brain surface extractor (BSE) [14], brain extraction tool (BET) [2], 3dIntracranial [15], and MRI watershed from FreeSurfer [16]. For extracting the brain, an atlas is used to define which brain extraction algorithm or combination of extractors works best defining the brain in each anatomic region.

In summary, different brain extraction approaches have been developed; however, they have their own drawbacks. Some of them give better results when removing non-brain tissue while losing some brain parts, and others give better results when extracting the whole brain while keeping some non-brain tissue parts [17], [18]. Atlas-based approaches are very time consuming and their performance heavily depends on the registration accuracy between the atlas and the test subject, in addition to the difficulty of constructing an infant brain atlas [19]. Moreover, the majority of the existing techniques are developed to work for adult MR brain images and fail to accurately extract the brain from MR infant images due to the reduced contrast and higher noise [20]. The infant brain MRI extraction meets with challenges stemming from image noise, inhomogeneities, artifacts, and discontinuities of boundaries due to similar visual appearance of adjacent brain structures, see Fig. 1. Furthermore, accurate infant brain extraction contributes much to the analysis, treatment, and the early diagnosis of brain injury and disorder resulting from the infant prematurity.

II. METHODS

To overcome the aforementioned limitations, we present a hybrid framework, shown in Fig. 2, that possesses the ability to accurately extract brain tissue from infant MR brain images. The proposed framework integrates both stochastic and geometric approaches and consists of four basic steps: (*i*) bias correction, (*ii*) skull stripping, (*iii*) iso-surfaces generation, and
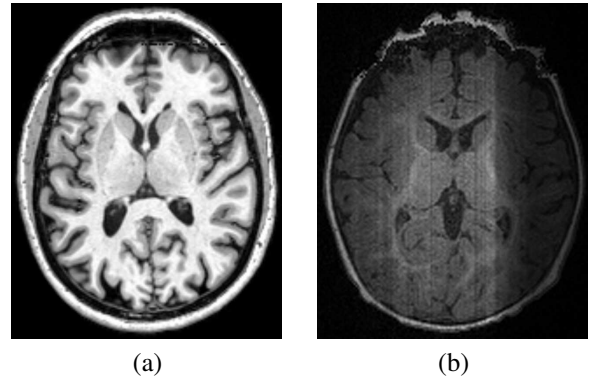

Fig. 1.   T1-weighted MRI scans for adult (a) and infant (b) brains.

(*iv*) final brain extraction using the visual appearance features of the MR brain images. Details of the proposed approach are outlined in the following sections.

A. Bias Correction

Illumination non-uniformity of infant brain MRIs, which is known as bias field, limits the accuracy of the existing brain extraction approaches. Therefore, to accurately extract the brain it is important to account for the low frequency intensity non-uniformity or inhomogeneity. In this work, we used a 3D generalized Gauss-Markov random field (GGMRF) model [21] that is applied after brain intensity normalization using the nonparametric approach proposed in [22]. This step reduces noise effects and removes (smooth) inconsistencies of the MRI data by accounting for the 3D spatially homogeneous pair-wise interactions between the gray levels of the MRI data. Namely, the gray level values $q \in \mathbf{Q} = \{0, \ldots, Q-1\}$ are considered as samples from a 3D GGMRF model [21] of measurements with the voxel 26-neighborhood. The continuity of q values of each brain MR scan is amplified by using their maximum A posteriori (MAP) estimates [21] and voxel-wise stochastic relaxation (iterative conditional mode (ICM) [23]):

$$\widehat{q}_s = \arg\min_{\widetilde{q}_s} \left[|q_s - \widetilde{q}_s|^\alpha + \rho^\alpha \lambda^\beta \sum_{r \in \nu_s} \eta_{s,r} |\widetilde{q}_s - q_r|^\beta \right] \quad (1)$$

where q_s and $\widetilde{q}_s$ are the original gray level values and their expected estimates, respectively, at the observed 3D location, $s = (x, y, z)$; ν_s is the 26-neighborhood system; $\eta_{s,r}$ is the GGMRF potential, and ρ and λ are scaling factors. The parameter $\beta \in [1.01, 2.0]$ controls the level of smoothing (e.g., $\beta = 2$ for smooth vs. $\beta = 1.01$ for relatively abrupt edges). The parameter $\alpha \in \{1, 2\}$ determines the Gaussian, $\alpha = 2$, or Laplace, $\alpha = 1$, prior distribution of the estimator. To demonstrate the effect of the first step of our framework, an example of the original, and bias-corrected (intensity normalization and GGMRF edge preservation) brain MR data is shown in Fig. 3 (a), and Fig. 3 (b,c), respectively.

B. Skull Stripping

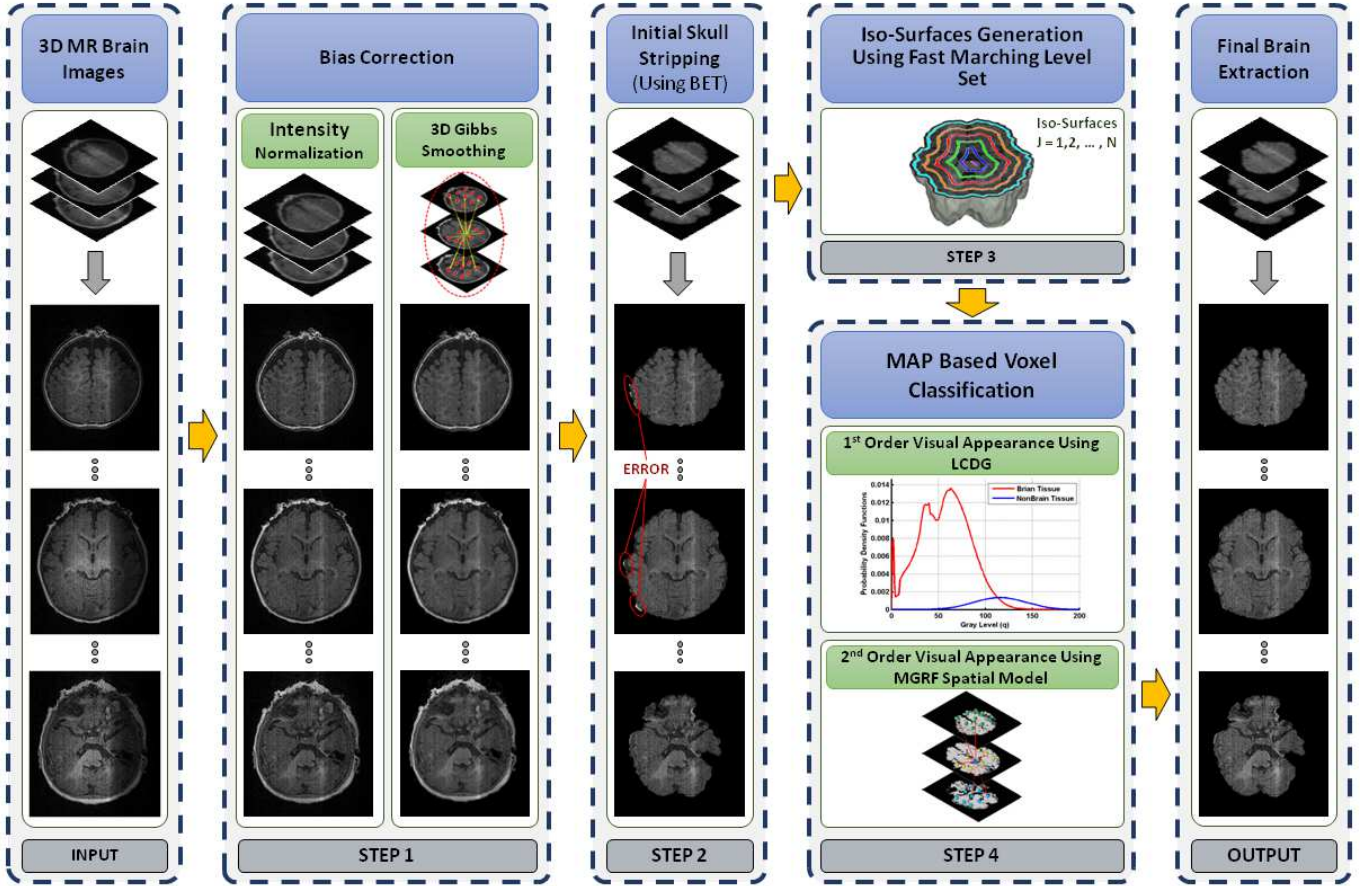The second step of the proposed framework after bias correction is to remove the non-brain tissue from the MR

Fig. 2. The basic steps of the proposed framework for brain extraction from infant MR brain data.

images. To accomplish this, we used the BET [2] with a small BET factor to minimize the loss of brain tissues, which uses a deformable model-based approach to remove the skull from brain MRIs. The initial brain extraction result of Fig. 3 (c) after the BET is shown in Fig. 3 (d). While the BET extracted the brain without losing any of its parts, it fails to remove all non-brain tissues. For some clinical applications, such as cortical thickness measurement, inaccurate skull stripping results in an over- or under-estimation of the thickness. Therefore, it is important to account for inaccurate skull stripping results after the BET step.

C. Visual Appearance-Guided Iso-Surfaces

In order to obtain more accurate brain extraction results, we propose an additional processing step based on the geometric features of the brain to account for BET's skull stripping errors. Since the non-brain tissues are brighter than brain tissue, this step exploits the visual appearance features of the MR brain data. Namely, an evolving iso-surface-based approach is proposed to remove the non-brain tissues, which is guided by the visual appearance features of the MR data (see Fig. 2, Steps #3&4). First, a set of nested, tangent surfaces (i.e., iso-surfaces) are generated by the fast marching level set (FMLS) approach [24], using the extracted brain from the BET step. In order to accurately classify MRI voxels as brain or non-brain, we need to accurately model MR data visual

appearance. To achieve this goal, we will use a joint Markov-Gibbs random field (MGRF) model, which is described below.

Let $\mathbf{Q} = \{0, \ldots, Q-1\}$ and $\mathbf{L} = \{$"brain", "non-brain"$\}$ denote sets of gray levels q and region labels L, respectively. Let $\mathbf{R}$ denote a 3D arithmetic lattice supporting a given grayscale image $\mathbf{g} : \mathbf{R} \to \mathbf{Q}$ to be segmented and its goal region map $\mathbf{m} : \mathbf{R} \to \mathbf{L}$. The 3D T1-weighted MR images, $\mathbf{g}$, and its map, $\mathbf{m}$, are described with the following joint probability model:

$$P(\mathbf{g}, \mathbf{m}) = P(\mathbf{g}|\mathbf{m})P(\mathbf{m}) \tag{2}$$

where $P(\mathbf{m})$ is an unconditional probability distribution of maps, and $P(\mathbf{g}|\mathbf{m})$ is a conditional distribution of the images given the map. The ultimate goal is to accurately estimate $P(\mathbf{g}|\mathbf{m})$ and $P(\mathbf{m})$, which are described next.

1) First-order visual appearance ($P(\mathbf{g}|\mathbf{m})$): To accurately approximate the marginal probability distributions of the brain and non-brain tissue, the empirical gray level distribution of a given brain data is precisely approximated with a linear combination of discrete Gaussians (LCDG) with positive and negative components [25]. The LCDG restores brain and non-brain transitions more accurately than a conventional mixture of only positive Gaussians, thus yielding a better initial map $\mathbf{m}$ formed by voxel-wise classification of the image gray values. Next the LCDG is explained in more details.
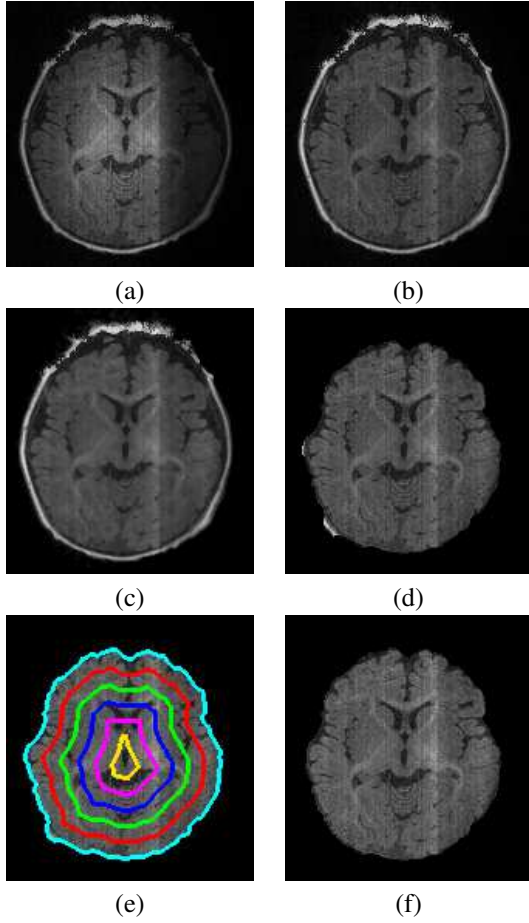
Fig. 3. Step-wise brain extraction using our framework: (a) the original MR image, (b) the bias-corrected image, (c) the GGMRF-edge preserved image obtained with $\rho = 1$, $\lambda = 5$, $\beta = 1.01$, $\alpha = 2$, and $\eta_{s,r} = \sqrt{2}$, (d) the extracted brain using BET [2], (e) the iso-surfaces used to remove non-brain tissues, and (f) the final extracted brain.

Let $\boldsymbol{\Psi}_\theta = (\psi(q|\theta) : q \in \mathbf{Q})$ defines a discrete Gaussian (DG)[1] where $\theta = (\mu, \sigma)$, integrating a continuous 1D Gaussian density with mean μ and variance σ^2 over successive gray level intervals [25]. The LCDG with two dominant positive DGs and $M_\mathrm{p} \geq 2$ positive and $M_\mathrm{n} \geq 0$ negative subordinate DGs is defined as [25]:

$$P_{\mathbf{w},\boldsymbol{\Theta}}(q) = \sum_{i=1}^{M_\mathrm{p}} w_{\mathrm{p}:i}\psi(q|\theta_{\mathrm{p}:i}) - \sum_{j=1}^{M_\mathrm{n}} w_{\mathrm{n}:j}\psi(q|\theta_{\mathrm{n}:j}) \quad (3)$$

where all the weights $\mathbf{w} = [w_{\mathrm{p}:i}, w_{\mathrm{n}:j}]$ are non-negative and meet an obvious constraint $\sum_{i=1}^{M_\mathrm{p}} w_{\mathrm{p}:i} - \sum_{j=1}^{M_\mathrm{n}} w_{\mathrm{n}:j} = 1$. All the LCDG parameters, including the numbers of DGs, are estimated from the mixed empirical distribution to be modeled using the modified expectation-maximization (EM)-based algorithm introduced in [26].

The marginal intensity distributions of the MR infant images have two dominant modes: one mode for brain tissues and

[1]A Discrete Gaussian (DG) $\boldsymbol{\Psi}_\theta = (\psi(q|\theta) : q \in \mathbf{Q})$ with $\theta = (\mu, \sigma^2)$ is defined as $\psi(q|\theta) = \Phi_\theta(q + 0.5) - \Phi_\theta(q - 0.5)$ for $q = 1, \ldots, Q - 2$, $\psi(0|\theta) = \Phi_\theta(0.5)$, and $\psi(Q-1|\theta) = 1 - \Phi_\theta(Q - 1.5)$ where $\Phi_\theta(q)$ is the cumulative Gaussian function with the mean μ and the variance σ^2.

a second mode for non-brain tissues. Figure 4 illustrates the basic steps to build the LCDG models of both modes. First, the marginal empirical probability distribution of the input grey level images (Fig. 4(a)) are collected (Fig. 4(b)). Then, the obtained empirical distribution is approximated with a mixture of two positive DGs relating each to a dominant mode (Fig. 4(c)). Second, the deviations between the empirical and the estimated distribution (Fig. 4(d)) are approximated with the alternating "subordinate" components of the LCDG described in [24]. Finally, the obtained positive and negative subordinate mixtures (Fig. 4(f)) are added to the dominant mixture yielding the final mixed LCDG model (Fig. 4(g)), which is partitioned into two LCDG-submodels (one per class, Fig. 4(h)) by associating the subordinate DGs with the dominant terms so that the misclassification rate is minimal [25].

2) Second-order visual appearance ($P(\mathbf{m})$): In order to overcome noise effect and to ensure segmentation homogeneity, the spatial interactions between the region labels of a brain map $\mathbf{m}$ are also taken into account using the popular Potts MGRF model. This model is identified using the nearest voxels' 26-neighbors (as shown in Fig.(5(a)) and analytical bi-valued Gibbs potentials (as shown in Fig.(5(b)) because only the coincidence of the labels is taken into account. The MGRF model is defined by [27] as:

$$P(\mathbf{m}) \propto \exp \sum_{(x,y,z)\in\mathbf{R}} \sum_{(\xi,\zeta,\kappa)\in\nu_s} \mathbf{V}(m_{x,y,z}, m_{x+\xi,y+\zeta,z+\kappa}) \quad (4)$$

where $\mathbf{V}$ is the bi-value Gibbs potential, that depends on whether the nearest pair of labels are equal or not:

$$V = \begin{cases} V(\lambda, \lambda') = V_{\mathrm{eq}} & \text{if} \quad \lambda = \lambda' \\ V(\lambda, \lambda') = V_{\mathrm{ne}} & \text{if} \quad \lambda \neq \lambda' \end{cases} \quad (5)$$
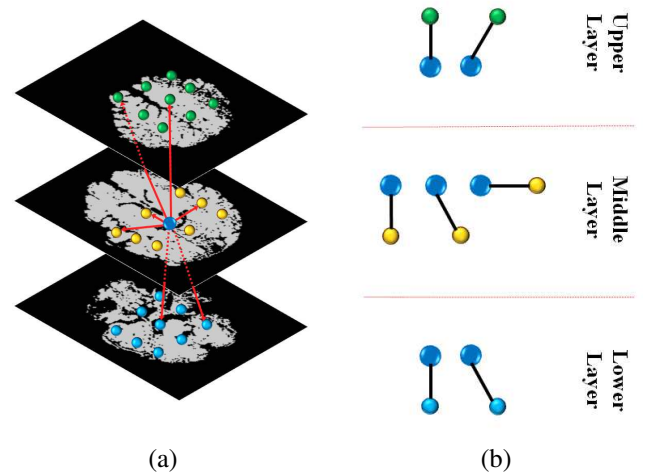

Fig. 5. A graphical illustration for the 3D neighborhood system (a) and a sample of the different pair-wise cliques for the 2nd-order MGRF (b).

Let $f_{a,\mathrm{eq}}(\mathbf{m})$ denote the relative frequency of the equal label pairs in the equivalent voxel pairs $\{((x, y, z), (x+\xi, y+\zeta, z+\kappa)) : (x, y, z), (x + \xi, y + \zeta, z + \kappa) \in \mathbf{R}; (\xi, \zeta, \kappa) \in \nu_s\}$. The initial $\mathbf{m}$ results in approximate analytical maximum likelihood potentials estimates [27]:
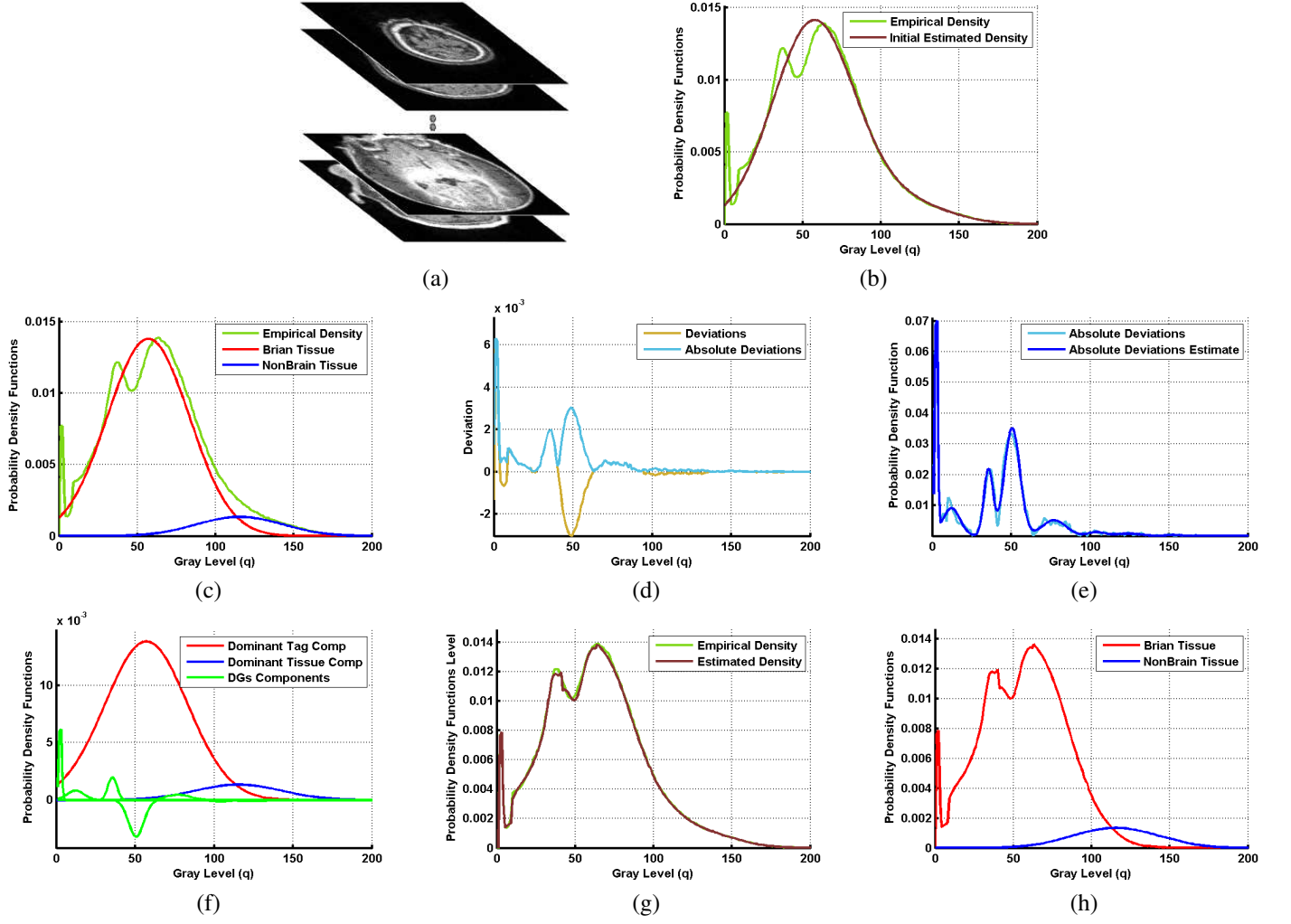
Fig. 4. Typical MR infant brain images (a); and estimated density (b) using only two dominant Gaussian components (c), deviation between empirical and estimated densities (d), estimated density of absolute deviation (e), LCDG components (f), final estimated density (g), and the final estimated marginal density for each class (h).

$$V_{\text{eq}} = -V_{\text{ne}} \approx 2f_{\text{eq}}(\mathbf{m}) - 1 \qquad (6)$$

that allow for computing the voxel-wise probabilities $p_{x,y,z}(m_{x,y,z} = \lambda)$ of each label $\lambda \in \mathbf{L}$. In total, Algorithm 1 summarizes the basic steps of the proposed brain extraction framework. For completeness, the analytical estimation of the bi-valued Gibbs potentials is driven in the Appendix A.

III. PERFORMANCE EVALUATION METRICS

The performance of the proposed framework was evaluated using three performance metrics: (*i*) the Dice similarity coefficient (DSC) [28], (*ii*) the 95-percentile modified Hausdorff distance (MHD) [29], and (*iii*) the absolute brain volume difference (ABVD). The following subsections explain the three metrics in more detail.

A. Dice similarity coefficient (DSC)

The dice similarity coefficient (DSC) characterizes the agreement between the segmented and ground truth objects (as seen in Fig. 6). The DSC measure is given from [28] as:

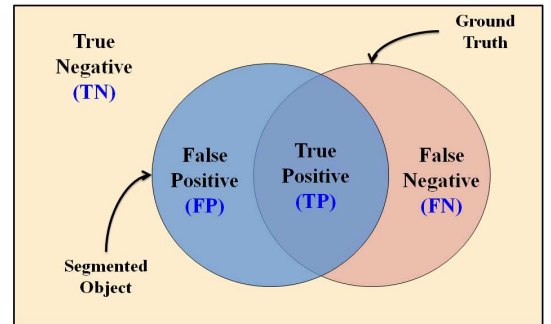$$DSC = \frac{2TP}{2TP + FP + FN} \qquad (7)$$

Fig. 6. Segmentation errors calculation between the segmented and ground truth objects for the determination of the dice similarity coefficient (DSC).

where TP, FP, and FN denote the true positive, false positive, and false negative respectively. Higher DSC values indicate

Algorithm 1 Proposed Brain Extraction Approach

1) Correct the bias of the MR brain data.
   a) Brain intensity normalization [22].
   b) GGMRF edge preservation [21].
2) Strip the skull using BET [2].
3) Estimate the LCDG models for brain and non-brain tissues using Step 2 results.
4) Form an initial $\mathbf{m}$ by voxel-wise classification using LCDG models found in Step 3.
5) Estimate analytically the Gibbs potentials for the pairwise MGRF model of $\mathbf{m}$ to identify the MGRF probability.
6) Calculate the distance map inside the binary mask obtained from BET using FMLS [24].
7) Generate a set of N iso-surfaces (Fig. 3 (e)) using the distance map calculated in Step 6.
8) while $j \leq N$
   a) Select the jth iso-surfacer and classify its voxels using a Bayes classifier combining the first and second-order visual appearance features.
   b) Are all the voxels on the selected iso-surfaces classified only as brain tissue?
      - No $\longrightarrow$ **Go to Step 8 (a)**.
      - Yes $\longrightarrow$ **Break**
9) Apply connected component analysis to obtain the final results.

better segmentation, which means that the results match the ground truth better than results with lower DSC values. A DSC value of 0 indicates no overlap and a DSC value of 1 indicates ideal segmentation (or agreement).

B. Modified Hausdorff distance (MHD)

In order to measure the error distance between the segmented and ground truth objects, we used the modified hausdorff distance (MHD). The Hausdorff distance (HD) [29] from a set A_1 to a set A_2 is defined as the maximum distance of the set A_1 to the nearest point in the set A_2 (as shown in Fig. 7):

$$H(A_1, A_1) = \max_{c \in A_1} \{ \min_{e \in A_2} \{ d(c,e) \} \} \qquad (8)$$

where c and e denote points of set A_1 and A_2 respectively, and $d(c,e)$ is the Euclidean distance between c and e.
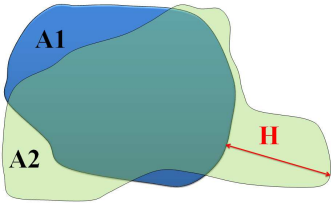

Fig. 7. A schematic illustration for the Haussdorf distance (HD) calculation.

The bidirectional HD between the segmented region SR and its ground truth GT is defined as:

$$H_{Bi}(GT, SR) = max\{H(GT, SR), H(SR, GT)\} \qquad (9)$$

In this paper, we use the 95th-perecntile bidierictional HD as a metric that measures the segmentation accuracy, which is also known as the modified Hausdorrf Distance (MHD).

C. Absolute brain volume difference (ABVD)

In addition to the DSC and the MHD, we have used the absolute brain volume difference (ABVD) as a third metric for measuring the segmentation accuracy. The ABVD is the percentage volume difference between the segmentation and the ground truth as seen in Fig. 8.
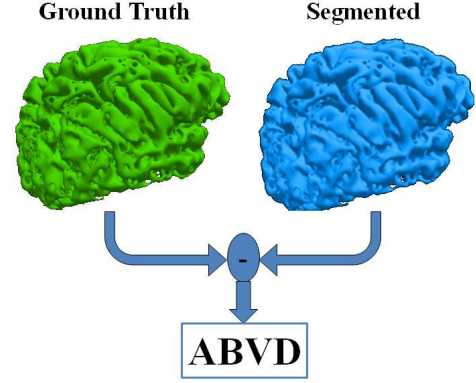

Fig. 8. 3D schematic illustration for the absolute brain volume difference (ABVD) estimation.

IV. EXPERIMENTAL RESULTS

In order to assess the robustness and performance of the proposed framework, we applied it to 300 T1-weighted MR infant brain data sets which were obtained from the Infant Brain Imaging Study (IBIS) [30], and evaluated its accuracy using 9 data sets with known manually segmented ground truth that were obtained by an MR expert. MR data was acquired at 3T and consists of T1- and T2-weighted MR images of infants scanned at approximately 5-9 months old with voxel size of $1 \times 1 \times 1$ mm^3.

A step-wise brain extraction using the proposed approach for a selected axial cross-section of one subject is demonstrated in Fig. 3. The input MR image (Fig. 3(a)) is first bias corrected (intensity normalized Fig. 3 (b)) and applied to the 3D GGMRF [21] edge preservation (Fig. 3 (c)). This is followed by an initial brain extraction using BET [2] (Fig. 3 (d)). Then, the proposed iso-surfaces based approach is employed to achieve the final segmentation as shown in Fig. 3 (f). It is clear from the results in Fig. 3 that the proposed framework provides more accurate infant brain extraction than BET. More segmentation results for different cross-sections from different subjects are shown in Fig. 9.

To highlight the advantage of the proposed framework we compared its performance to four widely-used brain extraction tools: the infant brain extraction and analysis toolbox (iBEAT) [31], the brain surface extractor (BSE) [14], the brain extraction tool (BET) [2], and the BET2 [32]. The comparative accuracy of the proposed approach versus the iBEAT, BSE, BET, and BET2 techniques on representative images for 3

TABLE I
COMPARATIVE ACCURACY OF OUR APPROACH VS. THE METHODS IN [2], [14], [31], [32] BY THE DSC, MHD, AND ABVD ON 9 DATA SETS WITH
AVAILABLE GROUND TRUTH ("SD "– STANDARD DEVIATION).

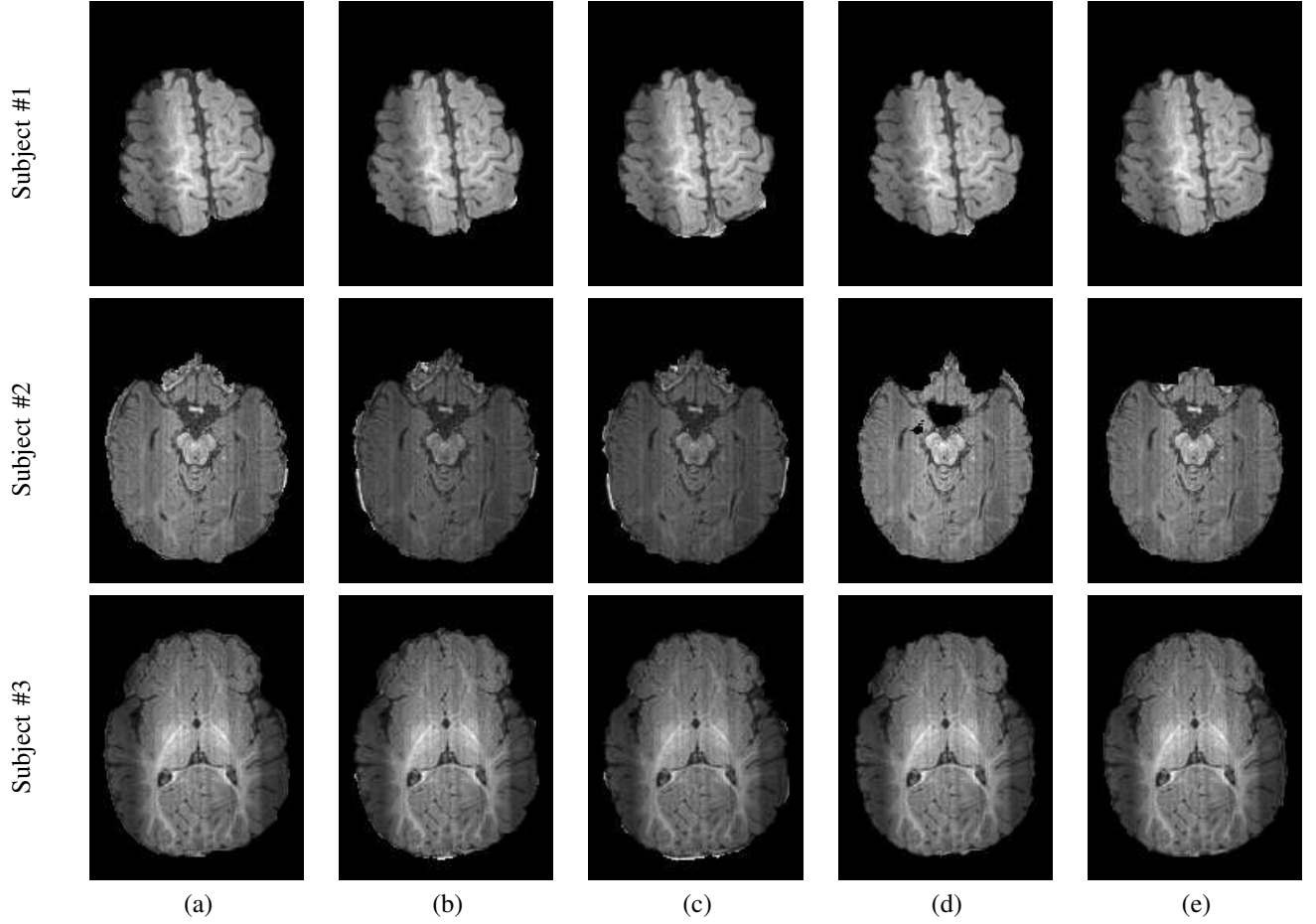|	Evaluation Metric					
	DSC (%)		MHD (mm)		ABVD (%)	
Method	Mean±SD	p-value	Mean±SD	p-value	Mean±SD	p-value
OUR	95.86±0.77	——	6.32±2.26	——	3.76±2.52	——
iBEAT [31]	94.30±2.47	0.0448	9.95±4.98	0.0179	6.84±5.25	0.0292
BSE [14]	93.17±1.44	0.0001	13.13±5.75	0.0007	5.64±2.11	0.0118
BET2 [32]	91.83±3.63	0.0049	13.80±6.74	0.0075	10.78±8.73	0.0137
BET [2]	91.80±3.42	0.0035	14.13±7.20	0.0099	10.58±8.33	0.0119

Fig. 10. Comparative brain extraction results for three independent subjects using (a) our approach, (b) BET [2], (c) BET2 [32], (d) BSE [14], and (f) iBEAT [31].

subjects is shown in Fig. 10. As demonstrated in Fig. 10 and the 3D extracted brains shown in Fig. 11, our approach extracted the brain tissue more accurately compared with the other approaches. The lower performance of the BET [2] could be caused by its sensitivity to image noise and inhomogeneity, because this method relies only on voxels' intensity changes and does not account for spatial voxel interactions. On the other hand, the BET2 approach [2] slightly improves the brain extraction accuracy compared with the BET one. However, unlike the BET and our approach, the BET2 technique requires both T1-and T2-weighted MR images. Moreover, BSE [14] succeeds in accurately removing the skull but it removes small parts from the brain tissues as well, which may lead to inaccurate results for some clinical application (e.g. cortical thickness under-estimation). The iBEAT performs multiple complementary brain extractions by using a meta-algorithm, including BET and BSE. However, Table I shows that our approach performs notably better, according to the higher DSC and ABVD values and lower MHD values. Table I compares our approach with the iBEAT, BSE, BET, and BET2, based on the DSC, MHD, and ABVD metrics. All metrics were obtained by comparing brain extraction results against the 9
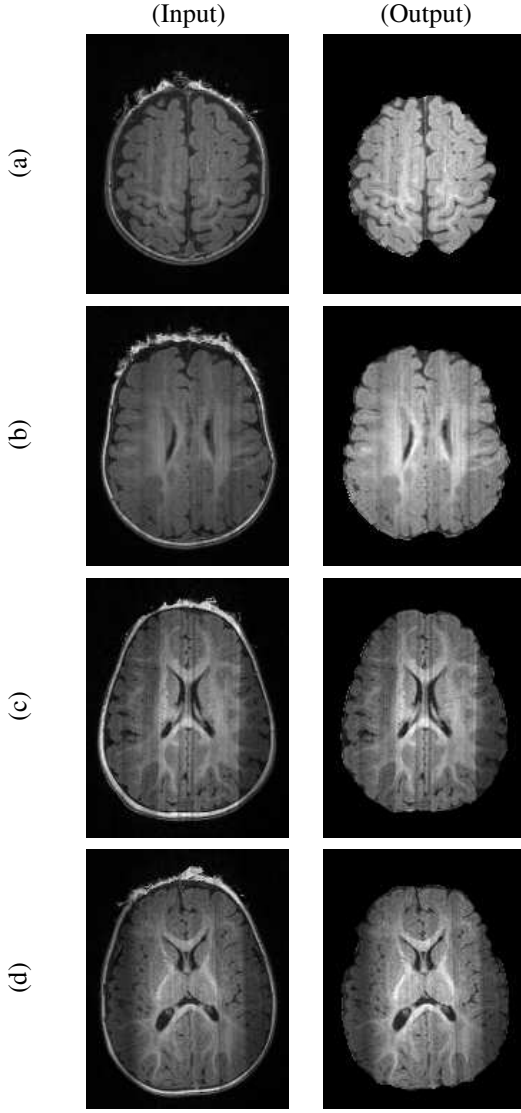
(Input) (Output)

(a)

(b)

(c)

(d)

Fig. 9. More segmentation results for different cross-sections from different subjects showing reliable brain extraction using the proposed approach.

data sets with available ground truth segmentation. As demonstrated in Table I, the mean DSC, MHD, and ABVD values for our framework are 95.86±0.77%, 6.32±2.26 mm, and 3.76±2.52%, respectively, which confirm the high accuracy of our approach. Statistical significance of the better performance of our approach with respect to other methods is confirmed by the paired t-tests (p-values are less than 0.05).

V. Conclusions and Future Work

In conclusion, this paper has introduced a novel framework for automated extraction of the brain from 3D infant MR images. Our experiments show that the fusion of stochastic and geometric models of the brain MRI data leads to more accurate brain extraction, when compared with widely-used brain extraction tools: iBEAT, BSE, BET, and BET2. The results were evaluated using the Dice similarity coefficient (DSC), 95-percentile modified Hausdorff distance (MHD), and the absolute brain volume difference (ABVD) on 9 infant MR brain data sets. A future extension of this work would be analyzing the extracted brain and testing these measurements

to characterize physiological processes and disease entities or to characterize disease severity.

Appendix

Analytical Estimation of the bi-valued Gibbs Potentials Let $\mathbf{Q} = \{0, \ldots, Q-1\}$ and $\mathbf{L} = \{0, \ldots, L-1\}$ denote sets of gray levels q and region labels k, respectively. Here, Q is the number of gray levels and K is the number of image modes, i.e. peaks in the gray level frequency distribution, e.g., for a bimodal image, $L = 2$. We assume that each dominant image mode corresponds to a particular class of objects to be found in the image.

Let $\mathbf{R} = \{(x, y, z) : 0 \leq x \leq X - 1, 0 \leq y \leq Y - 1, 0 \leq z \leq Z - 1\}$ be a 3D (x, y, z)-arithmetic grid supporting gray level images $\mathbf{g} : \mathbf{R} \to \mathbf{Q}$ and their region maps $\mathbf{m} : \mathbf{R} \to \mathbf{L}$. A two-level probability model of original images to segment and their desired region maps is given by a joint distribution $P(\mathbf{g}, \mathbf{m}) = P(\mathbf{m})P(\mathbf{g}|\mathbf{m})$ where $P(\mathbf{m})$ is an unconditional probability distribution of maps (2nd-order spatial Markov Gibbs random field (MGRF) model) and $P(\mathbf{g}|\mathbf{m})$ is a conditional distribution of images, given the map (1st-order intensity model). The Bayesian maximum *a posteriori* (MAP) estimate of the map $\mathbf{m}$, given the image $\mathbf{g}$:

$$\mathbf{m}^* = \arg \max_{\mathbf{m} \in \mathcal{X}} L(\mathbf{g}, \mathbf{m})$$

where $\mathcal{X}$ is the set of all region maps with labels $\lambda \in \mathbf{L}$ on $\mathbf{R}$, maximizes the log-likelihood function:

$$L(\mathbf{g}, \mathbf{m}) = \frac{1}{|\mathbf{R}|} \left(\log P(\mathbf{g}|\mathbf{m}) + \log P(\mathbf{m}) \right) \quad (10)$$

To find this estimate, we need to select the 1st-order intensity model and 2nd-order spatial MGRF model and identify their parameters.

A. Unconditional Region Map Model

The simplest model of interdependent region labels is the MGRF with the nearest 26-neighborhood of each voxel. By symmetry considerations, we assume the Gibbs potentials are independent of relative orientation of voxel pairs, are the same for all classes, and depend only on whether the pair of labels are equal or not. Under these assumptions, it is the simplest auto-binomial model, the Potts one, being for a long time a popular region map model [33]–[36]. But unlike the conventional counterparts, its Gibbs potential is obtained analytically using the maximum likelihood estimator for a generic MGRF derived in [37]. The 26-neighborhood results in a family $\mathbf{C_N} = [\mathbf{c}_{x,y,z,\xi,\eta,\kappa} = ((x, y, z), (x+\xi, y+\eta, z+\kappa)) : (x, y, z) \in \mathbf{R}; (x+\xi, y+\eta, z+\kappa) \in \mathbf{R}; (\xi, \eta, \kappa) \in \nu_s]$ of the neighboring voxel pairs supporting the Gibbs potentials. The potentials are bi-valued because only the coincidence of the labels is taken into account: $V(\lambda, \lambda') = V_{\text{eq}}$ if $\lambda' = \lambda'$ and V_{ne} if $\lambda \neq \lambda'$. Then the MGRF model of region maps is as follows:

$$\begin{aligned} P(\mathbf{m}) &= \frac{1}{Z_{\mathbf{N}}} \exp \sum_{(x,y,z) \in \mathbf{R}} \sum_{(\xi,\eta,\kappa) \in \nu_s} V(m_{x,y,z}, m_{x+\xi,y+\eta,z+\kappa}) \\ &= \frac{1}{Z_{\mathbf{N}}} \exp \left(|\mathbf{C_N}| V_{\text{eq}} \left(2f_{\text{eq}}(\mathbf{m}) - 1 \right) \right) \end{aligned} \quad (11)$$
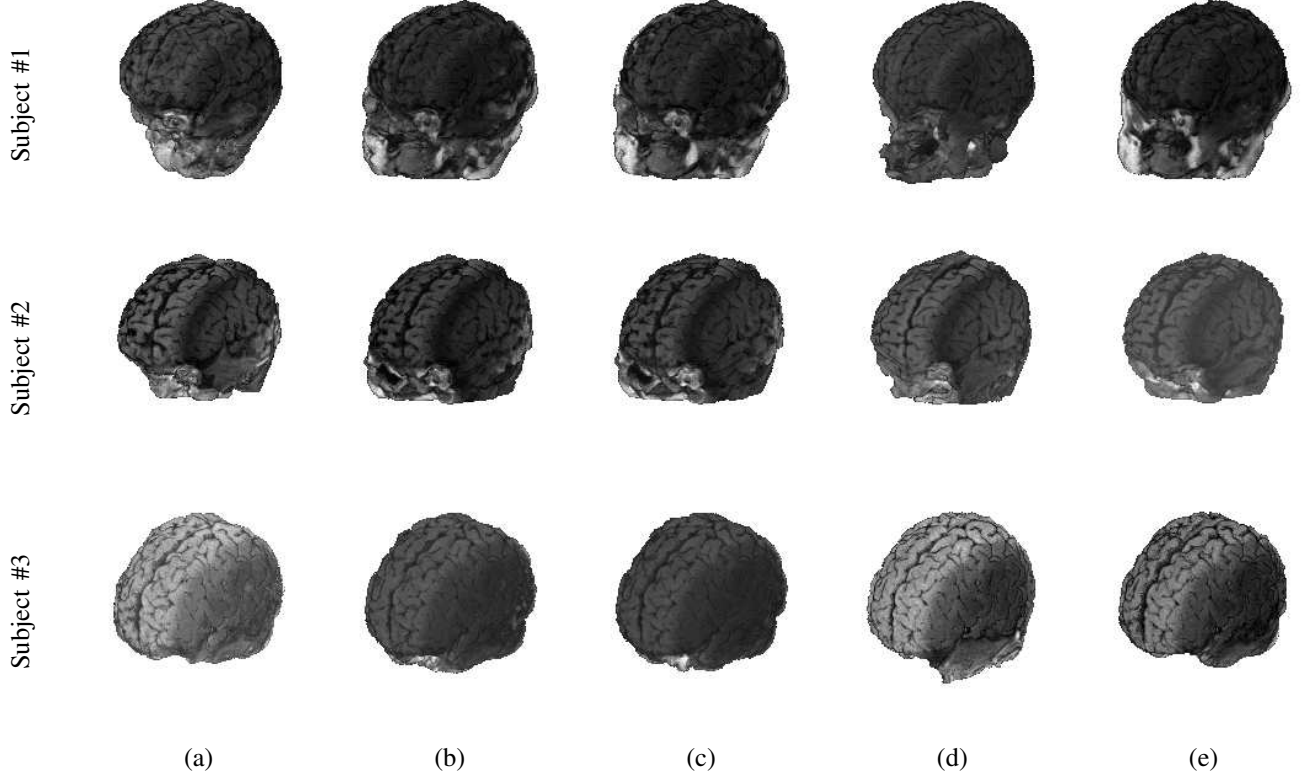
Fig. 11. 3D visualization of the segmented brain tissue for 3 different subjects using (a) our approach, (b) BET [2], (c) BET2 [32], (d) BSE [14], and (f) iBEAT [31].

where $|\mathbf{C_N}|$ is the cardinality of the family $\mathbf{C_N}$ and $f_{\text{eq}}(\mathbf{m})$ denotes the relative frequency of the equal labels in the voxel pairs of this family:

$$f_{\text{eq}}(\mathbf{m}) = \tfrac{1}{|\mathbf{C_N}|} \sum_{\mathbf{c}_{x,y,z,\xi,\eta,\kappa} \in \mathbf{C_N}} \delta(m_{x,y,z} - m_{x+\xi,y+\eta,z+\kappa}) \quad (12)$$

Here, $\delta()$ denotes the Kronecker delta function: $\delta(0) = 1$ and 0 otherwise. To identify the 2$^{\text{nd}}$-order MGRF model, we have to estimate only the potential value V_{eq} .

To compute the second term, $\frac{1}{|\mathbf{R}|} \log P(\mathbf{m})$, in Eq. (10) for a region map $\mathbf{m}$, we use the approximate partition function $Z_{\mathbf{N}}$ in [38] (see also [33], p.156) reduced in our case to:

$$
\begin{aligned}
Z_{\mathbf{N}} &\approx \exp\left(\sum_{x,y,z \in \mathbf{R}} \sum_{\xi,\eta,\kappa \in \nu_s} \sum_{\lambda \in \mathbf{L}} V(\lambda, m_{x+\xi,y+\eta,z+\kappa}) \right) \\
&= \exp\left(|\mathbf{C_N}| \sum_{\lambda \in \mathbf{L}} (V_{\text{eq}} f_\lambda(\mathbf{m}) - V_{\text{eq}}(1 - f_\lambda(\mathbf{m}))) \right) \\
&= \exp\left(V_{\text{eq}} |\mathbf{C_N}| (2 - L) \right)
\end{aligned}
$$

where $f_\lambda(\mathbf{m})$ is the marginal frequency of the label λ in the map $\mathbf{m}$. The above approximate partition function (which becomes too trivial for $L = 2$) results in the following approximation of the second term $\frac{1}{|\mathbf{R}|} \log P(\mathbf{m})$ in Eq. (10):

$$\varrho V_{\text{eq}}(2f_{\text{eq}}(\mathbf{m}) + L - 3) \approx 4V_{\text{eq}}(2f_{\text{eq}}(\mathbf{m}) + L - 3) \quad (13)$$

where $\varrho = \frac{|\mathbf{C_N}|}{|\mathbf{R}|} \approx |\nu_s| = 4$.

B. Identification of the 2$^{\text{nd}}$-order MGRF model

The approximate log-likelihood term in Eq. (13) is unsuitable for estimating the model parameter V_{eq} that specifies the Gibbs potential. Thus we identify the 2$^{\text{nd}}$-order MGRF model using a reasonably close first approximation of the maximum likelihood estimate (MLE) of V_{eq} derived for a given region map $\mathbf{m}^\circ$ in accord with [37] from the unconditional log-likelihood $L_u(\mathbf{m}^\circ|V_{\text{eq}}) = \frac{1}{|\mathbf{R}|} \log P(\mathbf{m}^\circ)$ of Eq. (11) with the exact partition function $Z_{\mathbf{N}} = \sum_{\mathbf{m} \in \mathcal{X}} \exp(V_{\text{eq}}\varrho|\mathbf{R}|(2f_{\text{eq}}(\mathbf{m}) - 1))$ where $\mathcal{X}$ is the parent population of region maps:

$$
\begin{aligned}
L_u(\mathbf{m}^\circ|V_{\text{eq}}) = \;& V_{\text{eq}}\varrho(2f_{\text{eq}}(\mathbf{m}^\circ) - 1) \\
& - \tfrac{1}{|\mathbf{R}|} \log \left(\sum_{\mathbf{m} \in \mathcal{X}} \exp(V_{\text{eq}}\varrho|\mathbf{R}|(2f_{\text{eq}}(\mathbf{m}) - 1)) \right)
\end{aligned}
$$

The approximation is obtained by truncating the Taylor's series expansion of $L(\mathbf{m}^\circ|V_{\text{eq}})$ in the close vicinity of zero potential, $V_{\text{eq}} = 0$, to the first three terms:

$$
\begin{aligned}
& L_u(\mathbf{m}^\circ|0) + V_{\text{eq}} \left. \tfrac{dL(\mathbf{m}^\circ|V_{\text{eq}})}{dV_{\text{eq}}} \right|_{V_{\text{eq}}=0} \\
& + \tfrac{1}{2}V_{\text{eq}}^2 \left. \tfrac{d^2 L_u(\mathbf{m}^\circ|V_{\text{eq}})}{dV_{\text{eq}}^2} \right|_{V_{\text{eq}}=0}
\end{aligned}
\quad (14)
$$

Because zero potential produces an independent random field (IRF) equiprobable region labels $\lambda \in \mathbf{L}$, the relative frequency of the equal pairs of labels over $\mathbf{C_N}$ has in this case the mean value $\frac{1}{L}$ and the variance $\frac{L-1}{L^2}$. Then the following

relationships hold:

$$\left.\frac{dL_u(\mathbf{m}^\circ | V_{\mathrm{eq}})}{dV_{\mathrm{eq}}}\right|_{V_{\mathrm{eq}}=0} = 2\varrho\left(f_{eq}(\mathbf{m}^\circ) - \tfrac{1}{L}\right)$$

$$\left.\frac{d^2 LE_u(\mathbf{m}^\circ | V_{\mathrm{eq}})}{dV_{\mathrm{eq}}^2}\right|_{V_{\mathrm{eq}}=0} = -4\varrho\frac{L-1}{L^2}$$

where $f_{eq}(\mathbf{m})^\circ$ is the relative frequency of the equal label pairs in the region map $\mathbf{m}^\circ$ specified in Eq. (12). The approximate likelihood of Eq. (14) results in the following MLE of V_{eq} for a given map $\mathbf{m}^\circ$:

$$V_{\mathrm{eq}} = \frac{L^2}{2(L-1)}\left(f_{\mathrm{eq}}(\mathbf{m}^\circ) - \frac{1}{L}\right) \qquad (15)$$

This relationship allows for computing the potentials of the Potts model for each current region map obtained by the Bayesian classification based on the estimated low-level image model. For bimodal images ($L = 2$), the value V_{eq} is estimated as:

$$V_{\mathrm{eq}} = 2f_{\mathrm{eq}}(\mathbf{m}^\circ) - 1 \qquad (16)$$

REFERENCES

[1] A. J. van der Kouwe, T. Benner, D. H. Salat, and B. Fischl, "Brain morphometry with multiecho mprage," *Neuroimage*, vol. 40, no. 2, pp. 559–569, 2008.

[2] S. M. Smith, "Fast robust automated brain extraction," *Human Brain Mapping*, vol. 17, no. 3, pp. 143–155, 2002.

[3] J.-X. Liu, Y.-S. Chen *et al.*, "Accurate and robust extraction of brain regions using a deformable model based on radial basis functions," *Journal of Neuroscience Methods*, vol. 183, no. 2, pp. 255–266, 2009.

[4] H. Wendland, "Piecewise polynomial, positive definite and compactly supported radial functions of minimal degree," *Advances in computational Mathematics*, vol. 4, no. 1, pp. 389–396, 1995.

[5] A. H. Zhuang, D. J. Valentino, and A. W. Toga, "Skull-stripping magnetic resonance brain images using a model-based level set," *NeuroImage*, vol. 32, no. 1, pp. 79–92, 2006.

[6] C. Baillard, P. Hellier, and C. Barillot, "Segmentation of brain 3D MR images using level sets and dense registration," *Medical Image Analysis*, vol. 5, no. 3, pp. 185–194, 2001.

[7] S. A. Sadananthan, W. Zheng, M. W. Chee, and V. Zagorodnov, "Skull stripping using graph cuts," *NeuroImage*, vol. 49, no. 1, pp. 225–239, 2010.

[8] H. Zhang, J. Liu, Z. Zhu, and H. Li, "An automated and simple method for brain MR image extraction," *Biomedical Engineering Online*, vol. 10, no. 1, p. 81, 2011.

[9] K. Somasundaram and T. Kalaiselvi, "Automatic brain extraction methods for T1 magnetic resonance images using region labeling and morphological operations," *Computers in Biology and Medicine*, vol. 41, no. 8, pp. 716–725, 2011.

[10] K. K. Leung, J. Barnes, M. Modat, G. R. Ridgway, J. W. Bartlett, N. C. Fox, and S. Ourselin, "Brain MAPS: an automated, accurate and robust brain extraction technique using a template library," *Neuroimage*, vol. 55, no. 3, pp. 1091–1108, 2011.

[11] J. E. Iglesias, C.-Y. Liu *et al.*, "Robust brain extraction across datasets and comparison with publicly available methods," *IEEE Transactions on Medical Imaging*, vol. 30, no. 9, pp. 1617–1634, 2011.

[12] F. Segonne, A. Dale *et al.*, "A hybrid approach to the skull stripping problem in MRI," *Neuroimage*, vol. 22, no. 3, pp. 1060–1075, 2004.

[13] D. E. Rex, D. W. Shattuck *et al.*, "A meta-algorithm for brain extraction in MRI," *NeuroImage*, vol. 23, no. 2, pp. 625–637, 2004.

[14] D. W. Shattuck and R. M. Leahy, "Brainsuite: an automated cortical surface identification tool," *Medical Image Analysis*, vol. 6, no. 2, pp. 129–142, 2002.

[15] B. D. Ward, "Intracranial segmentation," *Biophysics Research Institute, Medical College of Wisconsin, Milwaukee, WI*, 1999.

[16] A. M. Dale, B. Fischl, and M. I. Sereno, "Cortical surface-based analysis: I. Segmentation and surface reconstruction," *Neuroimage*, vol. 9, no. 2, pp. 179–194, 1999.

[17] D. W. Shattuck, G. Prasad, M. Mirza, K. L. Narr, and A. W. Toga, "Online resource for validation of brain segmentation methods," *NeuroImage*, vol. 45, no. 2, pp. 431–439, 2009.

[18] C. Fennema-Notestine *et al.*, "Quantitative evaluation of automated skull-stripping methods applied to contemporary and legacy images: Effects of diagnosis, bias correction, and slice location," *Human Brain Mapping*, vol. 27, no. 2, pp. 99–113, 2006.

[19] F. Shi, Y. Fan, S. Tang, J. H. Gilmore, W. Lin, and D. Shen, "Neonatal brain image segmentation in longitudinal MRI studies," *Neuroimage*, vol. 49, no. 1, pp. 391–400, 2010.

[20] A. U. Mewes, P. S. Hüppi *et al.*, "Regional brain development in serial magnetic resonance imaging of low-risk preterm infants," *Pediatrics*, vol. 118, no. 1, pp. 23–33, 2006.

[21] C. Bouman and K. Sauer, "A generalized gaussian image model for edge-preserving MAP estimation," *IEEE Transactions on Image Processing*, vol. 2, no. 3, pp. 296–310, 1993.

[22] N. J. Tustison, B. B. Avants *et al.*, "N4ITK: improved N3 bias correction," *IEEE Transactions on Medical Imaging*, vol. 29, no. 6, pp. 1310–1320, 2010.

[23] J. Besag, "On the statistical analysis of dirty pictures," *Journal of the Royal Statistical Society. Series B (Methodological)*, pp. 259–302, 1986.

[24] D. Adalsteinsson, "A fast level set method for propagating interfaces," Ph.D. dissertation, Citeseer, 1994.

[25] A. El-Baz *et al.*, "Precise segmentation of 3-D magnetic resonance angiography," *IEEE Transactions on Biomedical Engineering*, vol. 59, no. 7, pp. 2019–2029, 2012.

[26] A. Farag, A. El-Baz, and G. Gimel'farb, "Precise segmentation of multimodal images," *IEEE Transactions on Image Processing*, vol. 15, no. 4, pp. 952–968, 2006.

[27] A. El-Baz, "Novel stochastic models for medical image analysis," Ph.D. dissertation, University of Louisville, Louisville, KY, USA, 2006.

[28] D. Lee R, "Measures of the amount of ecologic association between species," *Ecology*, vol. 26, pp. 297–302, 1945.

[29] G. Gerig, M. Jomier, and M. Chakos, "Valmet: A new validation tool for assessing and improving 3D object segmentation," in *Medical Image Computing and Computer Assisted Intervention*, 2001, pp. 516–523.

[30] IBIS, "Infant brain imaging study," http://www.ibisnetwork.org/.

[31] F. Shi, L. Wang, Y. Dai, J. H. Gilmore, W. Lin, and D. Shen, "LABEL: Pediatric brain extraction using learning-based meta-algorithm," *NeuroImage*, vol. 62, no. 3, pp. 1975–1986, 2012.

[32] M. Jenkinson, M. Pechaud, and S. Smith, "BET2: MR-based estimation of brain, skull and scalp surfaces," in *Eleventh Annual Meeting of The Organization for Human Brain Mapping*, vol. 17, 2005.

[33] R. C. Dubes and A. K. Jain, "Random field models in image analysis," *Journal of Applied Statistics*, vol. 16, no. 2, pp. 131–164, 1989.

[34] G. L. Gimel'farb and A. Zalesny, "Probabilistic models of digital region maps based on Markov random fields with short-and long-range interaction," *Pattern Recognition Letters*, vol. 14, no. 10, pp. 789–797, 1993.

[35] R. W. Picard and I. M. Elfadel, "Structure of aura and co-occurrence matrices for the Gibbs texture model," *Journal of Mathematical Imaging and Vision*, vol. 2, no. 1, pp. 5–25, 1992.

[36] I. L. Dryden, M. R. Scarr, and C. C. Taylor, "Bayesian texture segmentation of weed and crop images using reversible jump Markov chain Monte Carlo methods," *Journal of the Royal Statistical Society: Series C (Applied Statistics)*, vol. 52, no. 1, pp. 31–50, 2003.

[37] G. Gimel'farb, *Image textures and Gibbs random fields*.

[38] J. Besag, "Spatial interaction and the statistical analysis of lattice systems," *Journal of the Royal Statistical Society. Series B (Methodological)*, pp. 192–236, 1974.